Measurement 283 (2026) 122156

Contents lists available at ScienceDirect

Measurement

journal homepage: www.elsevier.com/locate/measurement

On high-accuracy global corrosion parameter determination in metallic plates using multi-random-field inverse surrogates

Slawomir Koziel [a,b], Anna Pietrenko-Dabrowska [b], Beata Zima [c,*]

[a] Engineering Optimization & Modeling Center, Reykjavik University, 102 Reykjavik, Iceland
[b] Faculty of Electronics, Telecommunications and Informatics, Gdansk University of Technology, 80-233 Gdansk, Poland
[c] Faculty of Mechanical Engineering and Ship Technology, Gdansk University of Technology, 80-233 Gdansk, Poland

ARTICLE INFO

Keywords:
Guided ultrasonic waves
Nondestructive evaluation
Corrosion assessment
Inverse surrogate modeling
Stochastic corrosion morphology
Excitation frequency optimization

ABSTRACT

The accurate assessment of global corrosion characteristics in metal plates, particularly thickness loss and surface roughness, is critical for industries such as oil, marine, and energy. Recent advances using guided ultrasonic waves have enabled non-destructive evaluation of corroded structures; however, this task remains challenging due to complex interactions between wave propagation and spatially varying thickness profiles. The difficulty is further compounded by the inherently heterogeneous nature of real corrosion patterns, which introduces significant uncertainty in signal interpretation and limits the effectiveness of traditional physics-based identification methods. In this study, global corrosion parameters, including mean thickness reduction and thickness standard deviation, are reliably estimated using data-driven inverse surrogate models. Corrosion morphology is modeled as a stochastic field, while guided wave responses are generated via numerical simulations. The inverse framework maps features extracted from wave responses to corresponding corrosion parameters. A key challenge lies in the pronounced non-uniqueness of the problem, as infinitely many stochastic field realizations can yield identical statistical descriptors. To address this issue, a multi-random-field strategy is introduced, in which guided wave responses from multiple independent realizations are averaged and jointly analyzed. Extensive comparative studies show a clear improvement in prediction accuracy with as few as three random field realizations, with further significant gains observed for ten random field configurations. For the considered test cases, the relative mean absolute error was reduced to approximately 1.4% for thickness reduction estimation and 7.0% for standard deviation estimation. Across all cases, the proposed inverse modeling approach outperforms conventional time-of-flight-based identification methods derived from dispersion curve analysis. Although this research focuses on computational modeling, in practical applications, the proposed methodology can be readily implemented by repositioning the sensor network or excitation source, either laterally or rotationally.

1. Introduction

Guided ultrasonic waves have emerged as a powerful tool in structural health monitoring (SHM) due to their ability to propagate over long distances and their sensitivity to both material and geometrical properties of structures [1,2]. This sensitivity stems from the dispersive nature of guided waves, whose propagation characteristics-such as phase and group velocity, wavelength, and modal content-depend on the mechanical properties of the medium as well as the structural geometry, including thickness and boundary conditions [3,4]. In particular, their dependence on structural thickness makes them especially suitable for the inspection of plate-like components, where thickness variations can be directly linked to damage mechanisms such as corrosion [5–7]. Consequently, guided-wave-based techniques have been widely employed in non-destructive evaluation for detecting and quantifying structural degradation, including wall thinning and distributed damage [8–10].

At the same time, the strong dependence of guided wave propagation on structural geometry, while advantageous for damage detection, introduces significant challenges in solving the associated inverse problem, which consists in identifying the structural condition of a component based on the measured wave responses. In structures with

* Corresponding author.
E-mail addresses: koziel@ru.is (S. Koziel), anna.dabrowska@pg.edu.pl (A. Pietrenko-Dabrowska), beata.zima@pg.edu.pl (B. Zima).

https://doi.org/10.1016/j.measurement.2026.122156
Received 13 April 2026; Received in revised form 22 May 2026; Accepted 3 June 2026
Available online 8 June 2026

spatially varying properties, wave propagation is affected not only by global parameters but also by local variations in thickness, leading to complex phenomena such as scattering, mode conversion, and amplitude attenuation [11–14]. As a result, the relationship between measured signals and the underlying structural state becomes highly nonlinear and difficult to interpret, particularly in the presence of distributed damage.

Due to the complexity of the inverse problem, a variety of approaches have been proposed for the assessment of thickness distribution in plate-like structures based on guided wave signals. Many of these methods rely on simplified assumptions regarding the geometry of the inspected component, which enable analytical or semi-analytical treatment of the problem. For example, thickness estimation techniques based on time-of-flight measurements and dispersion curve analysis often assume uniform or effectively averaged thickness along the propagation path [9,15].

To investigate the influence of thickness variations on wave propagation, a number of studies have considered structures with simplified geometries, such as stepped plates [16,17] or plates with linearly varying thickness [18], where the effects of abrupt or gradual changes in geometry on wave characteristics can be systematically analyzed. Other approaches have employed parametric descriptions of plate geometry using predefined functional forms, allowing for the estimation of shape-related coefficients from measured signals [19–21].

More realistic representations of corroded structures have been achieved through the use of stochastic models, in which thickness variations are described using random fields capturing both global material loss and local surface irregularities [22–24]. While such approaches provide a more faithful representation of corrosion morphology, they also further increase the complexity of the inverse problem. Importantly, different realizations of such stochastic fields may share identical global statistical descriptors, such as mean thickness reduction and its standard deviation, while producing significantly different guided wave responses. Consequently, multiple corrosion profiles may correspond to similar signal characteristics, rendering the inverse problem of corrosion characterization inherently non-unique and ill-posed.

At the same time, conventional approaches to corrosion assessment, typically based on time-of-flight measurements and dispersion curve analysis, relate changes in wave velocity to thickness variations [15,19,21]. While effective for structures with uniform or weakly varying thickness, their applicability is limited in the presence of spatially distributed corrosion, where the concept of a single effective wave velocity becomes insufficient to capture the complexity of wave propagation. In such cases, the inferred parameters may be subject to significant uncertainty, particularly when local variations strongly influence the measured response.

To overcome the limitations of physics-based methods, data-driven approaches have been increasingly explored in recent years. Machine learning techniques have demonstrated strong potential in extracting damage-sensitive features from guided wave signals and establishing mappings between signal characteristics and structural parameters [25–27]. In particular, inverse modeling frameworks have been successfully employed to estimate defect properties and structural conditions directly from measured responses, without relying on simplified analytical assumptions [28,29]. However, most existing approaches operate on individual realizations of the structural response and do not explicitly account for the stochastic nature of corrosion morphology and the associated variability of guided wave signals.

Despite the growing interest in data-driven guided-wave-based corrosion assessment, several important limitations still remain insufficiently addressed. Most existing studies focus on localized defects or geometrically simplified damage scenarios, such as notches, cracks, wall thinning regions, or regular thickness variations. Although such configurations are valuable for understanding wave-damage interaction mechanisms, they do not fully represent the nature of corrosion developing over extended structural regions, where the thickness distribution is highly irregular and spatially heterogeneous. In practical corrosion scenarios, the guided wave response depends not only on the average material loss but also on the specific spatial arrangement of local thickness variations along the propagation path. Consequently, different corrosion morphologies may correspond to identical global statistical descriptors while simultaneously producing noticeably different wave responses.

This issue introduces a fundamental non-uniqueness into the inverse identification problem and significantly complicating the reliable estimation of corrosion parameters from guided-wave measurements [30]. Although stochastic descriptions of corrosion morphology have been previously considered in numerical and structural reliability studies, their implications for guided-wave-based inverse identification remain largely unexplored. In particular, there is still a lack of methodologies capable of explicitly accounting for the variability associated with the stochastic nature of corrosion fields while simultaneously identifying global corrosion descriptors directly from measured wave responses.

In this work, we address the inherent non-uniqueness of the inverse problem by introducing a multi-random-field inverse modeling framework for the identification of global corrosion parameters in metallic plates. The corrosion morphology is represented as a stochastic field characterized by its mean thickness reduction and standard deviation. Instead of relying on a single realization, multiple independent realizations of the corrosion field representing variable geometries but corresponding to the same statistical parameters are generated, and the resulting guided wave responses are jointly analyzed. By aggregating information across multiple realizations, the proposed approach effectively samples the stochastic space of corrosion morphologies, thereby improving the robustness and accuracy of the inverse mapping. It is important to emphasize that the proposed multi-random-field strategy also admits a clear physical interpretation. While in the numerical model multiple realizations of the stochastic field are generated, in practical applications a similar effect can be achieved by modifying the measurement configuration, for example, through repositioning of the sensors or the excitation source. Such changes result in different wave propagation paths across the structure, effectively sampling different spatial distributions of thickness along the propagation trajectories. Even small variations in sensor location may lead to noticeable differences in the encountered thickness profiles, and consequently, in the recorded wave responses. Therefore, multiple realizations considered in the proposed framework can be interpreted as representing different effective propagation scenarios associated with the same underlying statistical corrosion characteristics.

The main contributions of this study can be summarized as follows: (i) the introduction of a novel multi-random-field strategy for mitigating the inherent non-uniqueness of guided-wave-based inverse corrosion identification problems arising from stochastic corrosion morphology; (ii) the development of an inverse surrogate framework capable of estimating global corrosion descriptors directly from aggregated guided-wave response features; (iii) a systematic investigation of the influence of the number of stochastic field realizations on prediction robustness and estimation accuracy; and (iv) a comprehensive comparison with conventional time-of-flight-based identification approaches derived from dispersion analysis. The obtained results demonstrate that incorporating multiple statistically equivalent realizations substantially improves the stability and reliability of the inverse mapping, leading to significantly lower prediction errors even for a relatively small number of random field configurations.

2. Materials and methods

This part of the manuscript provides the details of the proposed multi-random-field inverse modeling approach to reliable estimation of corrosion parameters. The computational model is outlined in Section 2.1. The corrosion parameter prediction task is formulated in Section 2.2. Section 2.3 elucidates processing of guided wave response signals, whereas Section 2.4 defines the inverse regression model. The non-uniqueness issue is discussed at length in Section 2.5 along with the proposed mitigation technique. Section 2.6 briefly highlights the benchmark methodology, which is the time-of-flight-based parameter identification.

2.1. Modelling of corroded plate and computational model

In this study, corrosion is represented as a spatially distributed thickness variation over the plate domain. Rather than describing the surface deterministically, the corrosion morphology is modeled as a stochastic process to account for both global material loss and local geometric irregularities [31,32].

The plate thickness is defined as a spatially varying field $d(\boldsymbol{x})$, where $\boldsymbol{x} \in \Omega$ denotes a point in the plate mid-surface domain. The field is decomposed into a deterministic component corresponding to the average thickness and a stochastic fluctuation term describing corrosion-induced variability. Specifically, the thickness distribution is expressed as:

$$d(\boldsymbol{x}) = \overline{d} - h + s \cdot Z(\boldsymbol{x}) \tag{1}$$

where h denotes the mean thickness reduction, s represents the standard deviation of thickness, and $Z(\boldsymbol{x})$ is a zero-mean, unit-variance random field capturing spatial variability associated with corrosion roughness. The stochastic field $Z(\boldsymbol{x})$ is assumed to follow a Gaussian distribution and is characterized by a prescribed spatial correlation structure [33,34]. The correlation between two spatial locations depends on their distance and is controlled by a correlation length parameter, which determines the smoothness of the generated corrosion patterns.

To generate realizations of the random field, a truncated Karhunen–Loève expansion is employed. This approach enables efficient representation of spatial variability using a finite number of uncorrelated random variables, with the truncation level governing the effective dimensionality of the corrosion model [32,34]. In practice, a sufficiently large number of modes is retained to ensure accurate representation of the spatial statistics. The stochastic field is discretized on a regular grid and subsequently mapped onto the finite element mesh of the plate. The local thickness at each mesh node is obtained through interpolation of the generated field, and the nodal coordinates are adjusted accordingly to construct a three-dimensional geometry with spatially varying thickness.

Wave propagation in the corroded plate is simulated using a finite element (FE) model implemented in a transient dynamic framework. The structure is modeled as a three-dimensional solid with isotropic material properties. The computational domain corresponds to a square plate with dimensions $500 \times 500\ \text{mm}^2$ and nominal thickness of 4 mm. The FE discretization is performed using linear hexahedral elements with reduced integration. The mesh resolution is selected to ensure sufficient accuracy in capturing wave propagation phenomena, with the element size chosen relative to the shortest wavelength associated with the excitation frequency. Time integration is carried out using an explicit scheme, with the time step determined according to stability constraints. Guided waves are excited using a tone-burst signal with a prescribed central frequency of 100 kHz and windowing Hann function. The excitation is applied at a single point, and the resulting wave responses are recorded at multiple sensor locations distributed across the plate surface. Due to the dominance of the fundamental antisymmetric mode, the out-of-plane displacement component is used for further analysisAn example realization of the random field used to generate the irregular plate geometry, together with representative numerical results in the form of the propagating wavefield and the corresponding time-domain signals, is shown in Fig. 1.

The guided wave responses are acquired using 16 sensing paths distributed uniformly along a circular measurement configuration with a source-to-sensor distance of 150 mm. This arrangement was selected as a compromise between sufficient wave interaction with the corroded region and the need to avoid excessive influence of reflections, scattering, and wave attenuation. It should be emphasized, however, that the sensing configuration itself constitutes an important factor affecting the information content of the measured wavefield. In practical applications, the source-to-sensor distance, sensor arrangement, and available propagation paths may substantially influence the sensitivity of guided waves to distributed corrosion, as well as the robustness and interpretability of the extracted response features [35–37]. These aspects become particularly important in real engineering structures, where the sensing configuration is often constrained by structural complexity, accessibility limitations, and the presence of geometric discontinuities.

As presented in Fig. 1b and c, the spatial variability of the corrosion morphology directly affects the recorded guided wave responses

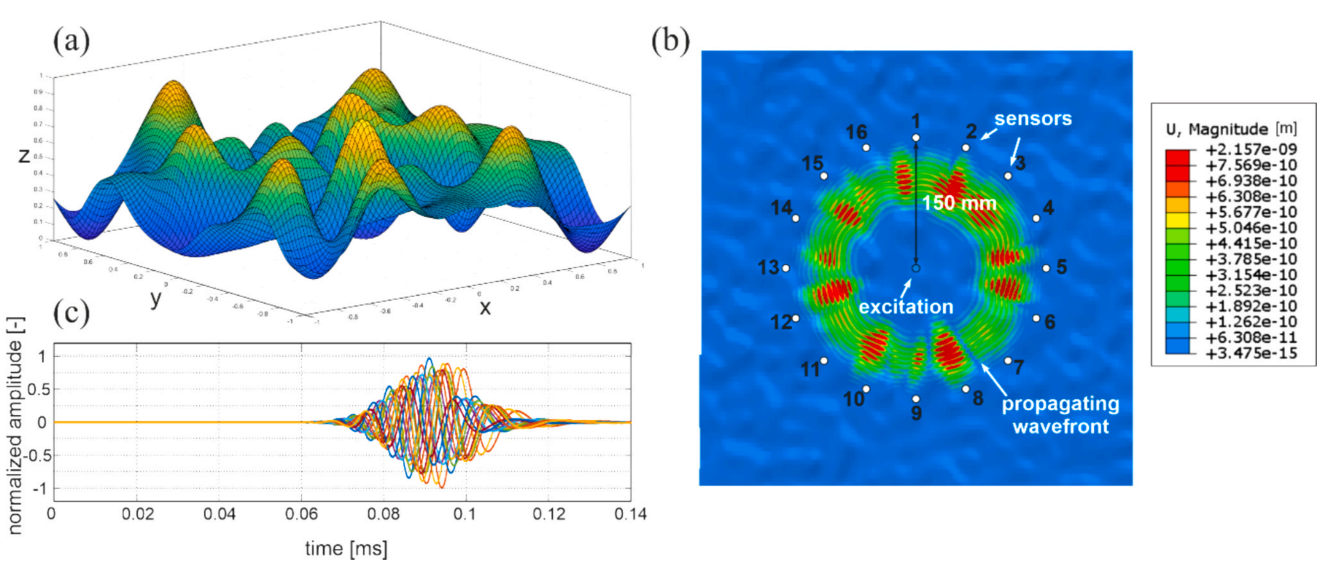

Fig. 1. Numerical simulations of wave propagation in corroded plate-like structures: (a) an example random field used to generate the geometry of the damaged plate; (b) visualization of wave propagation in a plate with non-uniform surface—wave excitation is applied at the center of the plate, while responses are recorded at 16 sensing points arranged along a circle with a radius of 150 mm from the source; (c) example time-domain signals recorded at the sensing points, illustrating pronounced asymmetry in the obtained responses.

through changes in wave velocity, attenuation, dispersion, and scattering phenomena. The acquired signals therefore constitute the basis for the subsequent feature extraction and inverse modeling procedure described in the following sections.

2.2. Problem statement

Our objective is to determine the global corrosion parameters, namely, thickness reduction h and the standard deviation s of thickness reduction, using the guided wave responses registered by sensors arranged on a circular pattern surrounding the excitation source. In this study $N_s = 16$ sensors are employed. The source excites a wave propagating towards the sensors at the frequency $f = 100$ kHz. As explained earlier, the wave pack properties (time of flight, pack width and amplitude) depend on the corrosion field morphology. The relationships between the guided wave response and the parameters h and s are captured using an inverse data-driven model, which is further used to predict these corrosion parameters given the sensor outputs.

The corrosion parameter space C is delimited by the lower and upper bounds $h_{\min}$ and $h_{\max}$ (for the thickness h) and $s_{\min}$, $s_{\max}$ (for the standard deviation s), i.e., $C = [h_{\min}\ h_{\max}] \times [s_{\min}\ s_{\max}]$. In the demonstration experiments of Section 3, we took the following values: $h_{\min} = 20\%$, $h_{\max} = 40\%$, $s_{\min} = 4\%$, and $s_{\max} = 20\%$. The guided wave response space, denoted as Y, will be defined in Section 2.3. The inverse model $S(\boldsymbol{y})$: $Y \rightarrow C$, $\boldsymbol{y} \in Y$, maps the response space into the corrosion parameter space, which allows for direct prediction of parameters h and s corresponding to a given sensor output. To ensure reliable prediction, it is imperative that the model is sufficiently accurate across the space Y, i.e., $||\boldsymbol{c}(\boldsymbol{y}) - S(\boldsymbol{y})||$ is within the acceptance limit, where $\boldsymbol{c}(\boldsymbol{y}) = [h(\boldsymbol{y})\ s(\boldsymbol{y})]$ are the "true" corrosion parameter values corresponding to $\boldsymbol{y}$. The predictive power of the inverse model will be evaluated using conventional metrics such as Mean Absolute Error (MAE), Relative MAE (RMAE), and Pearson correlation coefficient R (cf. Section 3).

One of the main problems in constructing the inverse model is the fact that there are infinitely many realizations of the stochastic corrosion field corresponding to the same pair of parameters h and s. This leads to strong non-uniqueness which translates into limited model's accuracy. This is because when building the model, the training data incorporates one specific realization of the corrosion morphology for each combination of h and s. The abovementioned non-uniqueness manifests itself as a numerical noise, and model identification effectively fits the noisy data. This issue will be discussed at length in Section 2.5 along with the proposed mitigation approach.

2.3. Signal processing

The computational model outlined in Section 2.1 produces waveforms $f_k(t)$, $k = 1, \ldots, N_s$, where t stands for time. The signals $f_k(t)$ consists of the fundamental response (a shifted and scaled copy of the excitation signal $e(t)$) and additional components associated with wave reflections and scattering, cf. Fig. 2(a). In this work, we only consider the amplitude-normalized primary response. For further processing, each sensor output is assigned three features related to the Gaussian-like envelope extracted to match the maxima $(t_{k.j}, y_{k.j})$, $j = 1, \ldots, K_k$, of $|f_k(t)|$. These include the mean μ, variance σ, and amplitude A. The extraction process has been elucidated in Fig. 3(a), whereas Fig. 2(b) provides its graphical illustration. However, instead of individual sensor features ($3N_s$ in total as in $\boldsymbol{v}_f = [A_1 \ldots A_{Ns}\ \mu_1 \ldots \mu_{Ns}\ \sigma_1 \ldots \sigma_{Ns}]^T$), it is more convenient to use statistical moments thereof as defined in Fig. 3(b), which—to certain extent—mitigate the non-uniqueness problem mentioned in Section 2.2.

2.4. Inverse model construction

The foundation of the inverse model is a set of training samples $\boldsymbol{c}_B^{(k)} = [h_B^{(k)}\ s_B^{(k)}]^T \in C$, $k = 1, \ldots, N_B$, and the associated feature vectors $\boldsymbol{v}_{s.B}^{(k)}$. Due to low dimensionality of the corrosion parameter space, the training points are allocated on a rectangular grid uniformly covering the ranges of interest, i.e., the interval $[h_{\min}\ h_{\max}] \times [s_{\min}\ s_{\max}]$. The feature vectors are extracted from the outcome of the simulation model (cf. Section 2.1). For validation, we use an independent set of testing points $\boldsymbol{c}_t^{(k)} = [h_t^{(k)}\ s_t^{(k)}]^T$, $k = 1, \ldots, N_t$, allocated on another rectangular grid, separate from that used for the training data.

The relationship between the mean propagation velocity and corrosion thickness is close to linear, which results from the fact that, over the corresponding portion of the dispersion curve, the dependence of group velocity on the considered thickness range can be reasonably approximated by a linear function. Consequently, a linear regression model is the most appropriate for representing the parameters h and s. Additionally, linear model smoothens out guided wave response variations due to the inherent randomness of the corrosion distribution field. Analytical formulation of the inverse model is

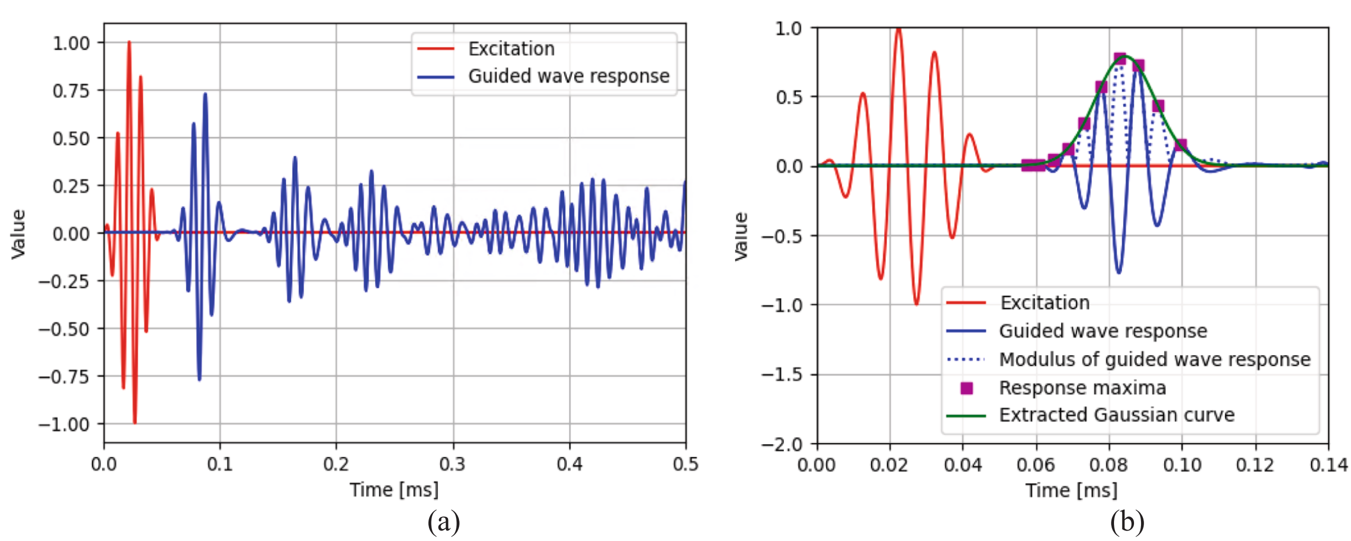

Fig. 2. Excitation signal and guided wave response: (a) excitation with complete response (fundamental and spurious parts, including wave reflections); (b) feature extraction by fitting a Gaussian curve to the local maxima of the sensor signal modulus. For individual sensors, we identify the time-wise center of the primary response μ, its temporal width σ, and the amplitude A.

$$G(t) = A\exp\left(-\left(\frac{t-\mu}{\sigma}\right)^2\right) \tag{F1}$$

Feature extraction: Solve least square regression problem

$$[A_k^*, \mu_k^*, \sigma_k^*] = \arg\min_{A,\mu,\sigma}\left\| \begin{bmatrix} G(t_{k.1}; A, \mu, \sigma) \\ \vdots \\ G(t_{k.K_k}; A, \mu, \sigma) \end{bmatrix} - \begin{bmatrix} y_{k.1} \\ \vdots \\ y_{k.K_k} \end{bmatrix} \right\| \tag{F2}$$

(a)

Feature vector: arithmetic means and standard deviations of individual sensor features A_k, μ_k, and σ_k, $k = 1, \ldots, N_s$:

$$\boldsymbol{v}_s = \left[\bar{A}\ \bar{\mu}\ \bar{\sigma}\ std(A)\ std(\mu)\ std(\sigma)\right]^T \tag{F3}$$

where

$$\bar{A} = \frac{\sum_k^{N_s} A_k^*}{N_s},\quad \bar{\mu} = \frac{\sum_k^{N_s} \mu_k^*}{N_s},\quad \bar{\sigma} = \frac{\sum_k^{N_s} \sigma_k^*}{N_s} \tag{F4}$$

$$std(A) = \sqrt{\frac{\sum_k^{N_s}(A_k^* - \bar{A})^2}{N_s - 1}},\quad std(\mu) = \sqrt{\frac{\sum_k^{N_s}(\mu_k^* - \bar{\mu})^2}{N_s - 1}},\quad std(\sigma) = \sqrt{\frac{\sum_k^{N_s}(\sigma_k^* - \bar{\sigma})^2}{N_s - 1}} \tag{F5}$$

(b)

Fig. 3. Feature extraction of sensor responses $f_k(t)$: (a) extraction process, (b) feature vector consisting of statistical moments of individual sensor features.

$$S(\boldsymbol{v}_s) = [L_{h.0}\ L_{s.0}] + \boldsymbol{v}_s^T\boldsymbol{L} \tag{2}$$

where the coefficients $L_{h.0}$, $L_{s.0}$, and a 6×2 matrix $\boldsymbol{L}$ are found by solving the least-square regression problems

$$S\left(v_{s.B}^{(k)}\right) = \left[h_B^{(k)} s_B^{(k)}\right], k = 1, \ldots, N_B \tag{3}$$

If $N_B > \dim(\boldsymbol{v}_s)$, i.e., when the system of equations (2) is over-determined, the coefficients can be found analytically as

$$\begin{bmatrix} L_{h.0}\ L_{s.0} \\ \boldsymbol{L} \end{bmatrix} = (\boldsymbol{A}^T\boldsymbol{A})^{-1}\boldsymbol{A}^T\boldsymbol{C}_B \tag{4}$$

where

$$\boldsymbol{A} = \begin{bmatrix} \begin{bmatrix} 1 \\ \vdots \\ 1 \end{bmatrix} & \boldsymbol{V}_s \end{bmatrix} \tag{5}$$

with $\boldsymbol{V}_s = [(\boldsymbol{v}_{s.B}{}^{(k)})^T\ (\boldsymbol{v}_{s.B}{}^{(k)})^T\ \ldots\ (\boldsymbol{v}_{s.B}{}^{(NB)})]^T$, and

$$\boldsymbol{C}_B = \begin{bmatrix} h_B^{(1)}\ s_B^{(1)} \\ \vdots \\ h_B^{(N_B)}\ s_B^{(N_B)} \end{bmatrix} \tag{6}$$

In Section 3, we will also use a second-order regression model $S_2(\boldsymbol{v}_s) = [L_{h.0}\ L_{s.0}] + \boldsymbol{v}_s^T\boldsymbol{L} + P(\boldsymbol{v}_s)^T\boldsymbol{L}_2$, where $P(\boldsymbol{v}_s)$ is a vector consisting of second-order monomials of response features, and $\boldsymbol{L}_2$ is a respective coefficient matrix. The identification of the model is similar to that of $S(\boldsymbol{v}_s)$, therefore, the details are omitted here.

2.5. Mitigating non-uniqueness: Multi-measurement approach

By convention, the training samples $\boldsymbol{c}_B{}^{(k)}$ for inverse model construction correspond to specific realization of the random corrosion field. However, as mentioned earlier, any specific pair of thickness reduction h and its standard deviation s correspond to an infinite number of distinct corrosion fields. This has been illustrated in Figs. 4 and 5 for

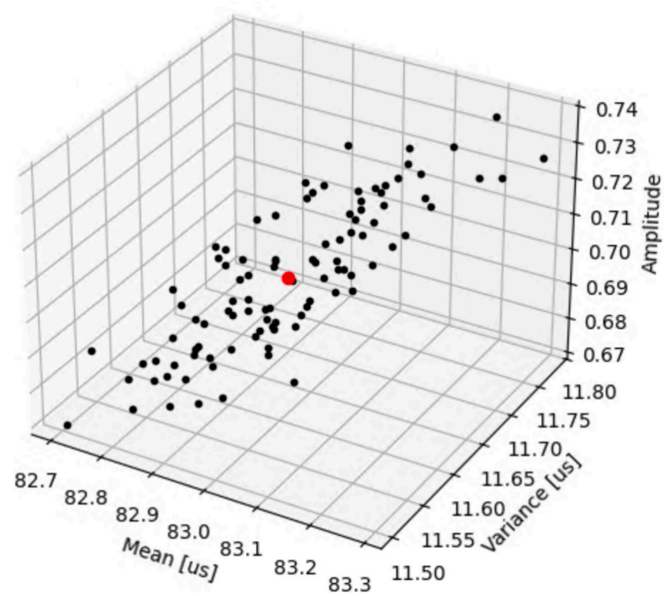

Fig. 4. Response features (first three entries of vector $\boldsymbol{v}_s$) for 100 different realizations of the stochastic corrosion field corresponding to h = 20% and s = 10%. The picture illustrates non-uniqueness of the inverse modeling problem. The red dot represents the geometric mean of the feature distribution set.

specific values of h and s. Additionally, Fig. 6 demonstrates the same problem at the level of individual sensors: depending on the corrosion morphology, the response features corresponding to each sensor vary, and so the mean values (at the level of the entire sensor network). For the complete training set, as illustrated in Fig. 7, the non-uniqueness problem manifests itself in the roughness of the training point distributions, which is particularly noticeable for the response amplitudes (the right-hand-side panel) but also the response variance. When the training points are generated using different realizations of the

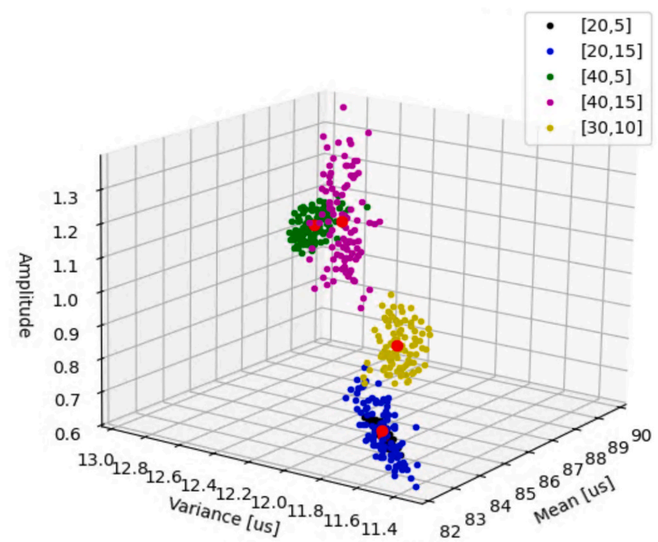

Fig. 5. Response features for 100 realizations of the stochastic corrosion field for five different corrosion parameters along with their geometric centers.

stochastic corrosion fields (blue *vs.* green dots), the emerging patterns are different. This is a practical challenge. On the one hand, the inverse model cannot be excessively complex because accurate representation of the training data is pointless given the fact that data acquired from other corrosion field realization would be different. In this context, simpler models (such as low-order polynomial ones) are preferred due to their ability to smooth out these variations. On the other hand, the non-uniqueness puts a fundamental limit on possible model accuracy as different realizations of the testing (or measurement) data lead to similar variations on the model's predictions.

In this study, the non-uniqueness problem is addressed by building the inverse model using multi-random-field training data. More specifically, the training samples $\mathbf{c}_B^{(k)} = [h_B^{(k)}\ s_B^{(k)}]^T \in C$ are obtained as arithmetic averages of data points acquired for multiple realizations of the corrosion fields corresponding to the same parameters h and s. For each pair $h_B^{(k)}$ and $s_B^{(k)}$, N_f random fields are generated and their corresponding feature vectors are extracted as $\mathbf{v}_{s.B.j}^{(k)}$, $j = 1, \ldots, N_f$. The averaged feature vectors are $\mathbf{v}_{s.B}^{(k)} = N_f^{-1}\Sigma_j \mathbf{v}_{s.B.j}^{(k)}$. As illustrated in Fig. 8, this has a profound effect on the training data distribution, which is noticeably regularized even for N_f as small as three, cf. Fig. 8(b). For $N_f = 10$, the effects are significant, as shown in Fig. 8(c). The averaging process is equivalent to estimating the geometric centers of the feature distribution sets illustrated in Figs. 4 and 5. The impact of multi-random-field approach on model performance metrics such as RMAE or correlation coefficient will be quantified in Section 3.

At this point, it should be emphasized, that improving the prediction accuracy also requires that the testing data (or measurement outcome in practical scenarios) must also be rendered in a multi-random-field fashion. While it is straightforward at the level of computational modeling, in practical experimental setup, it requires spatial relocation of sensors (or the excitation source), through lateral shifts or rotation. This is because any movement of sensors is equivalent to yielding a different realization of the corrosion field as the specific corrosion profile on the lines connecting the signal source and the sensors would alter accordingly.

2.6. Benchmark algorithm

For validation purposes, a reference method based on time-of-flight analysis of guided wave signals is employed. This approach is a standard technique used for thickness estimation in plate-like structures and will be used here as a baseline for comparison with the proposed inverse modeling framework.

The ToF-based procedure relies on estimating the propagation time of the incident wave packet between the excitation point and a set of sensors distributed over the structure. These measurements are used to determine the effective wave propagation characteristics, which are subsequently related to the structural thickness through dispersion relationships corresponding to the considered guided wave mode. The relationship between wave velocity and thickness is governed by the dispersion characteristics of guided waves, which are obtained numerically for the considered material properties and excitation frequency range. The mapping from velocity to thickness is performed using pre-computed dispersion data for the selected wave mode (Fig. 9).

It should be emphasized that the ToF-based method inherently assumes a uniform or weakly varying thickness along the wave propagation path [38]. In practice, this implies that the estimated wave velocity

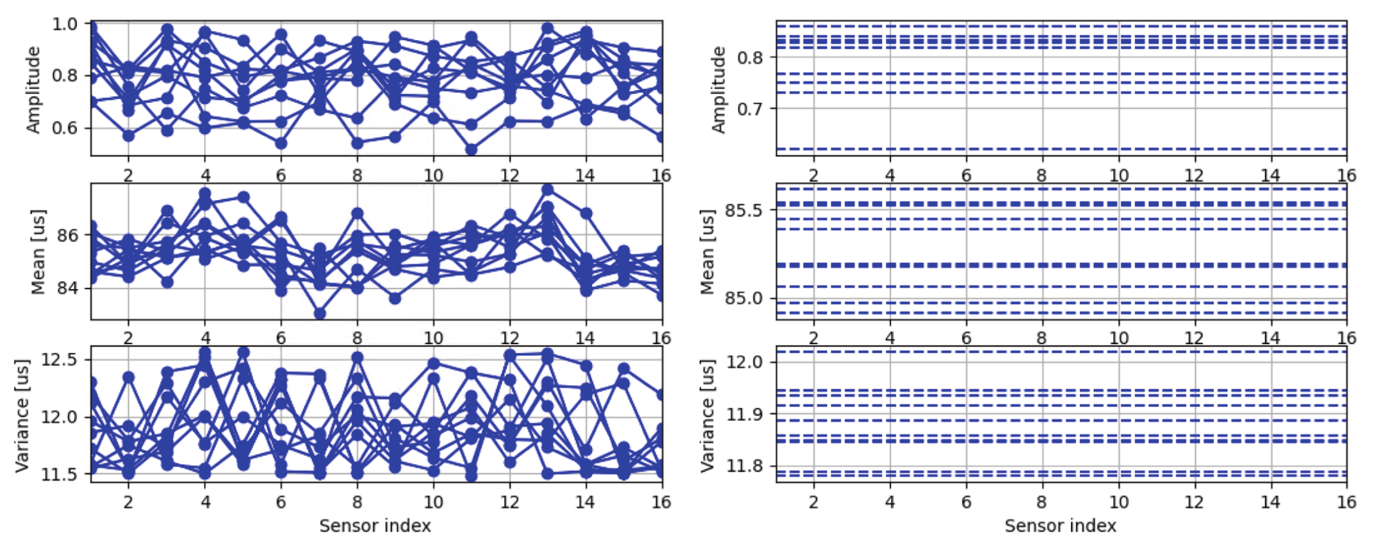

(a) (b)

Fig. 6. Preprocessed sensor signals for $N_s = 16$ and guided wave responses obtained for ten realizations of the stochastic corrosion fields corresponding to $h = 30\%$ and $s = 10\%$: (a) extracted response features for individual sensors, (b) mean values of features across the sensor set. The figure illustrates the variability of the guided wave responses associated with different realizations of the stochastic corrosion morphology.

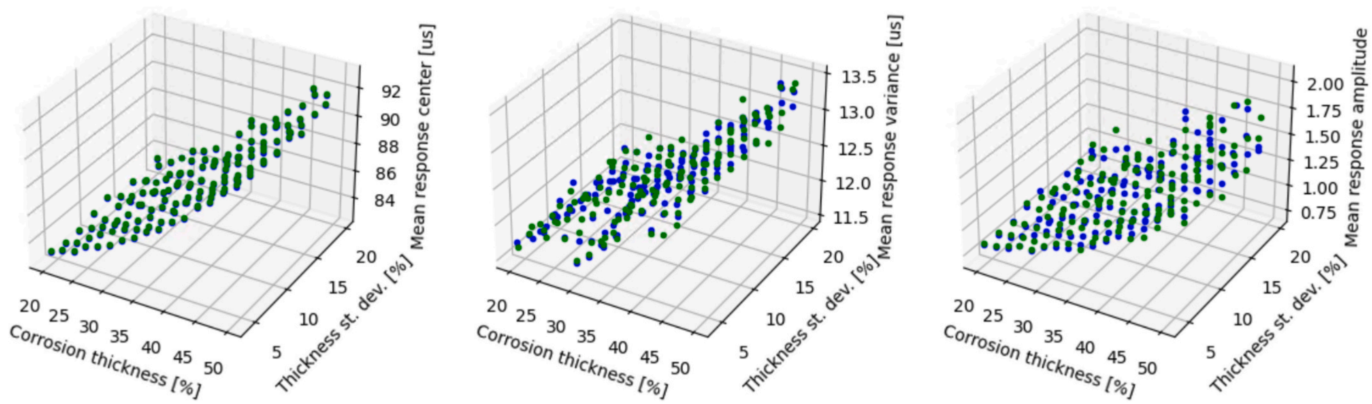

Fig. 7. Response features (mean response center – left, mean response variance – middle, mean response amplitude – right) corresponding to different corrosion parameters (h and s) distributed within the range of interest $[h_{\min}, h_{\max}] \times [s_{\min}, s_{\max}]$. Green and blue dots correspond to different realizations of the stochastic corrosion fields. Observe that the distributions for response variance and amplitude are significantly different due to the non-uniqueness issue illustrated in Figs. 4–6.

corresponds to an effective value averaged over the entire propagation trajectory. Consequently, the inferred thickness can be interpreted as a path-averaged quantity rather than a direct representation of the actual spatial distribution of material loss.

In the case of distributed corrosion, where thickness variations are spatially complex and exhibit stochastic characteristics, this assumption becomes only approximate. Different propagation paths may traverse regions with significantly different local thickness profiles, leading to variability in the recorded signals. As a result, the ToF-based estimates obtained from different sensing directions are generally inconsistent and reflect directional averaging effects rather than true local geometry.

This effect is further illustrated by the observed asymmetry of the recorded waveforms (cf. Fig. 1c), which indicates that wave propagation is strongly influenced by local variations in thickness and surface morphology. Consequently, each sensor measurement may lead to a different effective thickness estimate, even for the same global corrosion parameters.

3. Results

This section provides numerical verification of the proposed multi-random-field inverse modeling methodology. The predictive performance of the surrogate is quantified using standard metrics such as mean absolute error and correlation coefficients. We also investigate the effects of incorporating different numbers of random field realizations on the model's predictive power and compare our approach to the benchmark method (time-of-flight technique). The material is divided into three parts. The experimental setup is outlined in Section 3.1. Section 3.2 puts together the results. Section 3.3 summarizes the key observations.

3.1. Experimental setup

The inverse model is constructed using the dataset $\boldsymbol{c}_B{}^{(k)} = [h_B{}^{(k)}\ s_B{}^{(k)}]^T$, $k = 1, \ldots, N_B$, outlined in Section 2.5, and validated using the testing points $\boldsymbol{c}_t{}^{(k)} = [h_t{}^{(k)}\ s_t{}^{(k)}]^T$, $k = 1, \ldots, N_t$. In this study both datasets are subsets of the points allocated on a 16×9 grid, corresponding to $h \in \{20, 22, \ldots, 48, 50\}$, and $s \in \{4, 6, \ldots, 18, 20\}$. The training subset contains 40 points obtained for all combinations of $h \in \{20, 24, 28, 32, 36, 40, 44, 50\}$ and $s \in \{4, 8, 12, 16, 20\}$, whereas the testing subset encapsulates the remaining points from the original grid (114 samples in total).

The model predictive power is quantified using a Relative Mean Absolute Error (RMAE), a Mean Absolute Error (MAE), and the Pearson correlation coefficient (R), defined as follows:

$$RMAE = \frac{\frac{1}{n}\sum_{k=1}^{n}|x_k - y_k|}{\frac{1}{n}\sum_{k=1}^{n}x_k} \tag{7}$$

$$MAE = \frac{1}{n}\sum_{k=1}^{n}|x_k - y_k| \tag{8}$$

$$R = \frac{\sum_{k=1}^{n}(x_k - \bar{x})(y_k - \bar{y})}{\sqrt{\sum_{k=1}^{n}(x_k - \bar{x})^2 \sum_{k=1}^{n}(y_k - \bar{y})^2}} \tag{9}$$

where x_k and y_k are predicted and actual values, whereas $\bar{x}$ and $\bar{y}$ are their mean values.

3.2. Results and verification

The numerical results obtained for the benchmark approach (time-of-flight-based identification) and the proposed multi-random-field inverse modeling are encapsulated in Table 1. The predictive power of the inverse model rendered using single-random-field approach (or $N_f = 1$) is juxtaposed against the multi-field approach with different $N_f = 3$, 5, and 10. Furthermore, the linear model is compared to the quadratic one for the same numbers of random field realizations. Meanwhile, Figs. 10–14 illustrate the scatter plots for the techniques considered.

3.3. Discussion of results

The results obtained in this study provide clear evidence that the proposed inverse surrogate framework is highly effective for estimating global corrosion parameters in metallic plates. In all considered cases, the inverse-model-based approach yields markedly better prediction accuracy than the conventional time-of-flight-based methodology. This remains true even for the simplest variant of the surrogate, i.e., the linear model constructed using a single realization of the stochastic corrosion field. For this case, the obtained errors are already relatively low, with RMAE equal to 3.7% for thickness reduction h and 17.5% for the standard deviation s, accompanied by correlation coefficients of 0.983 and 0.844, respectively. These figures indicate that even a single-realization inverse model captures substantially more information from the guided wave responses than the benchmark approach based solely on effective wave velocity.

A central finding of this work is the demonstrated importance of multi-random-field averaging. Incorporating multiple realizations of the stochastic corrosion morphology, while keeping the same global parameters h and s, leads to a systematic reduction in prediction error and a simultaneous increase in correlation. For the linear model, averaging

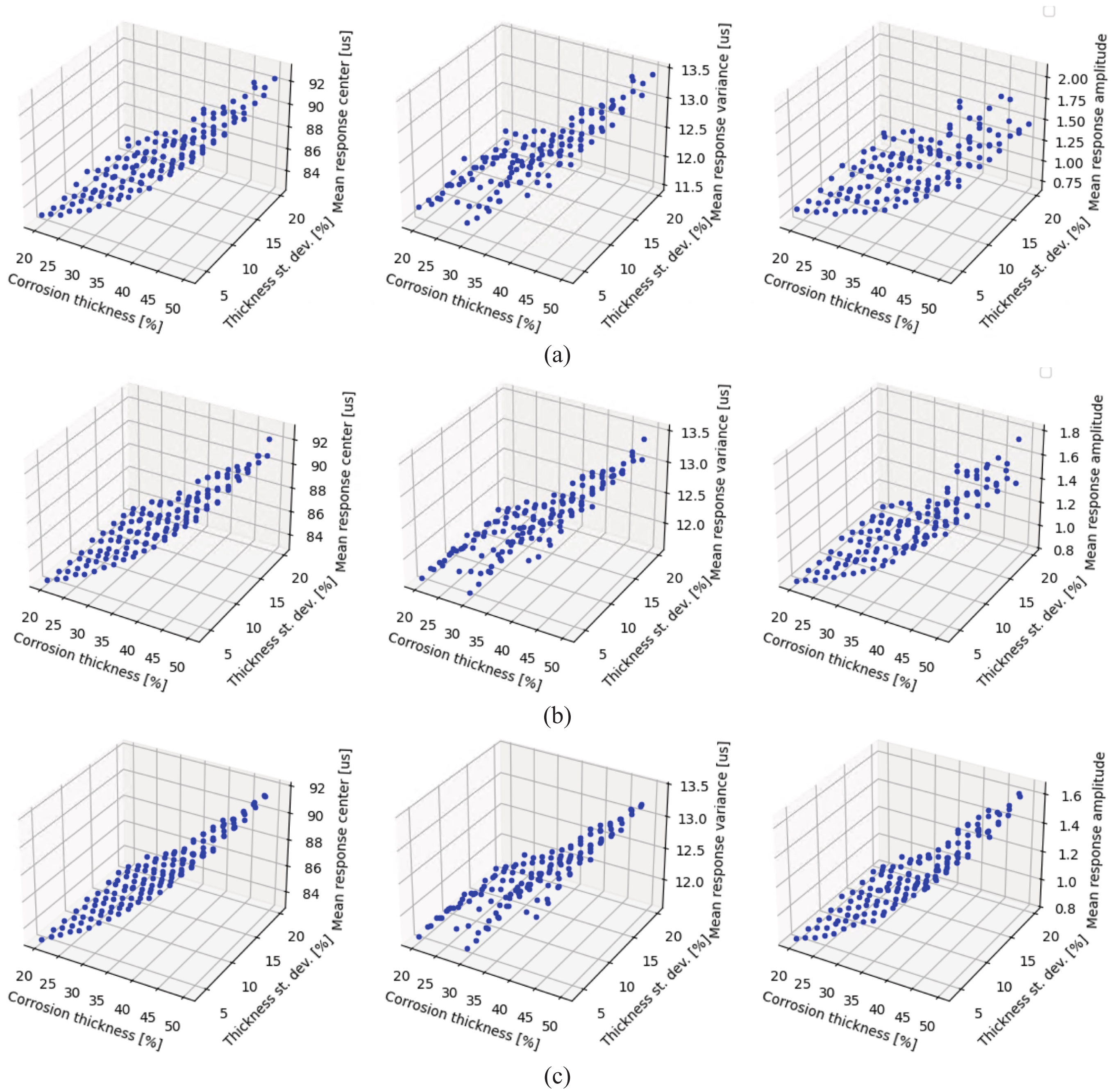

Fig. 8. Response features (mean response center – left, mean response variance – middle, mean response amplitude – right) corresponding to different corrosion parameters (h and s) distributed within the range of interest $[h_{\min}, h_{\max}] \times [s_{\min}, s_{\max}]$: (a) one random field realization per parameter pair, (b) average of three random field realizations, (c) average of ten random field realizations. Observe that increasing the number of random fields (per corrosion parameter pair) smoothens the surfaces facilitating a construction of the inverse model and mitigating the non-uniqueness issue.

over three realizations improves the RMAE for thickness reduction from 3.7% to 2.5%, while the corresponding MAE decreases from 1.3% to 0.9%, and the correlation coefficient increases from 0.983 to 0.993. For the standard deviation parameter s, the improvement is also significant, with RMAE reduced from 17.5% to 13.0%, MAE from 2.1% to 1.6%, and correlation increasing from 0.844 to 0.928. These results show that the proposed multi-random-field strategy is already highly beneficial at a relatively small ensemble size.

Further increasing the number of realizations to five leads to another noticeable improvement. In the case of the linear surrogate, the RMAE drops to 2.1% for h and 11.5% for s, while the MAE reaches 0.8% and 1.4%, respectively. At the same time, the correlation coefficients increased to 0.995 for the thickness reduction and 0.940 for the thickness standard deviation. This consistent improvement confirms that averaging over multiple realizations effectively suppresses realization-specific fluctuations in the response and allows the inverse model to better capture the underlying relationship between the measured signal features and the global corrosion parameters.

The best overall performance is obtained for the largest ensemble size considered, i.e., $N_f = 10$. For the linear surrogate, this already yields excellent results, with RMAE equal to 1.9% for h and 10.2% for s, and corresponding MAE values of 0.7% and 1.2%. The associated correlation coefficients, 0.996 and 0.955, indicate extremely strong agreement between the predicted and reference values. These results clearly

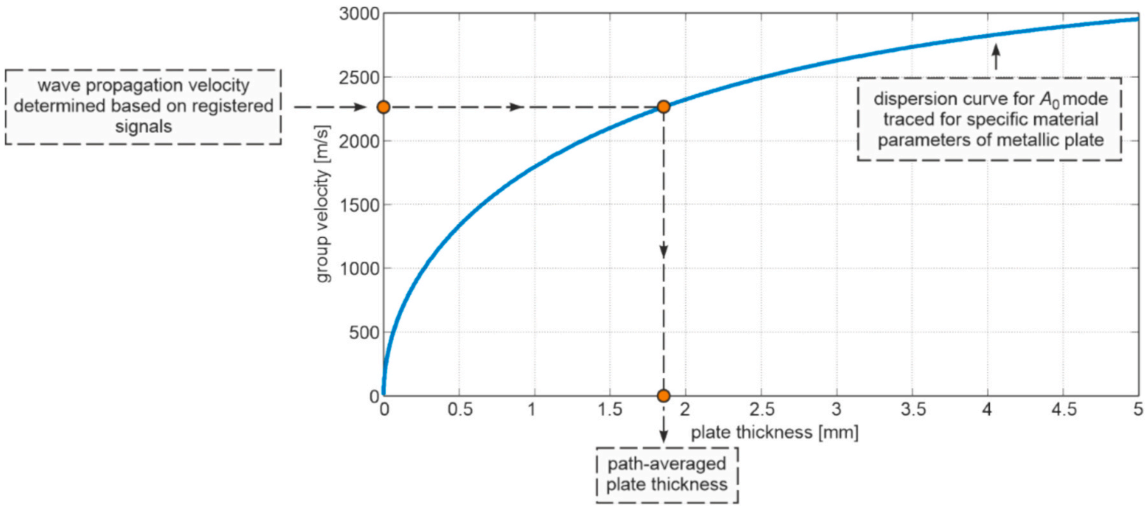

Fig. 9. Time-of-flight-based procedure for mean plate thickness estimation.

Table 1
Corrosion parameter prediction using the multi-random-field inverse model and benchmark.

Model	Accuracy metric					
	Thickness reduction h			Standard deviation s		
	RMAE[#]	MAE	R	RMAE[#]	MAE	R
Benchmark (time-of-flight-based identification)	18.1%	6.3%	0.732	38.4%	4.6%	0.447
Linear (single-random-field)	3.7%	1.3%	0.983	17.5%	2.1%	0.844
Linear (multi-random-field $N_f = 3$)	2.5%	0.9%	0.993	13.0%	1.6%	0.928
Quadratic (multi-random-field $N_f = 3$)	3.3%	1.1%	0.985	13.4%	1.6%	0.902
Linear (multi-random-field $N_f = 5$)	2.1%	0.8%	0.995	11.5%	1.4%	0.940
Quadratic (multi-random-field $N_f = 5$)	1.5%	0.5%	0.997	11.0%	1.3%	0.942
Linear (multi-random-field $N_f = 10$)	1.9%	0.7%	0.996	10.2%	1.2%	0.955
Quadratic (multi-random-field $N_f = 10$)	1.4%	0.5%	0.997	7.0%	0.9%	0.975

[#] RMAE expressed in percent is the relative error of estimating the percentage of h and s, also expressed in percent. Example: for RMAE = 5% and estimated h of 30%, the error is ± 1.5% (i.e., the true value is between 28.5% and 31.5%).

demonstrate that as the number of realizations increases, the inverse problem becomes effectively better conditioned, and the prediction of global corrosion parameters becomes more stable and reliable.

An important additional observation concerns the role of the surrogate model structure. The results indicate that the quadratic model does not provide a uniform improvement for all ensemble sizes. In particular, for $N_f = 3$, the quadratic surrogate performs worse than the linear one. For thickness reduction, the RMAE increases from 2.5% to 3.3%, the MAE from 0.9% to 1.1%, and the correlation drops from 0.993 to 0.985. A similar, although less pronounced, degradation is also observed for the standard deviation parameter. This behavior suggests that, for a relatively small number of realizations, the quadratic model possesses too many degrees of freedom relative to the amount of regularized information available in the training data. As a result, the model tends to fit realization-dependent fluctuations rather than the underlying trend, which leads to reduced generalization capability.

At the same time, the quadratic surrogate becomes advantageous once the number of realizations is sufficiently large. For $N_f = 5$, the quadratic model already outperforms the linear one in terms of thickness prediction, reducing the RMAE from 2.1% to 1.5% and the MAE from 0.8% to 0.5%, while slightly improving the correlation coefficient from 0.995 to 0.997. For the standard deviation s, the improvement is smaller but still visible. The most pronounced gains are obtained for $N_f = 10$, where the quadratic surrogate delivers the best results among all tested models. In this case, the RMAE is reduced to 1.4% for thickness

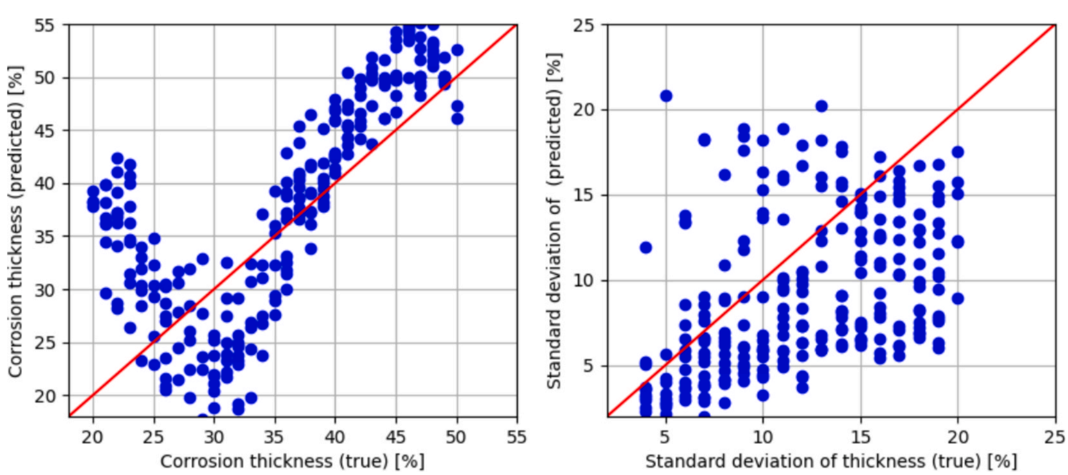

Fig. 10. Scatter plot for the benchmark technique. The solid line indicates the identity function.

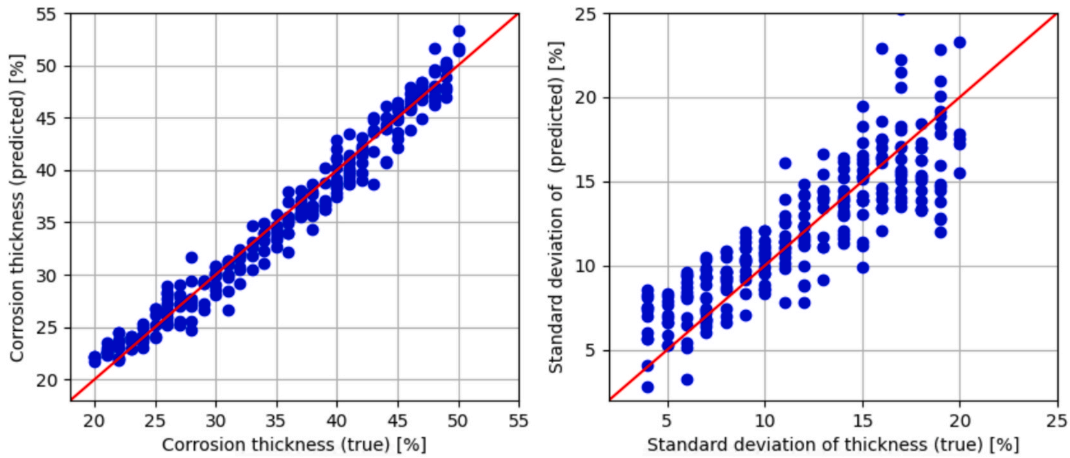

Fig. 11. Scatter plots for the corrosion parameter prediction techniques based on inverse model (single-random-field approach, or $N_f = 1$). The solid line indicates the identity function.

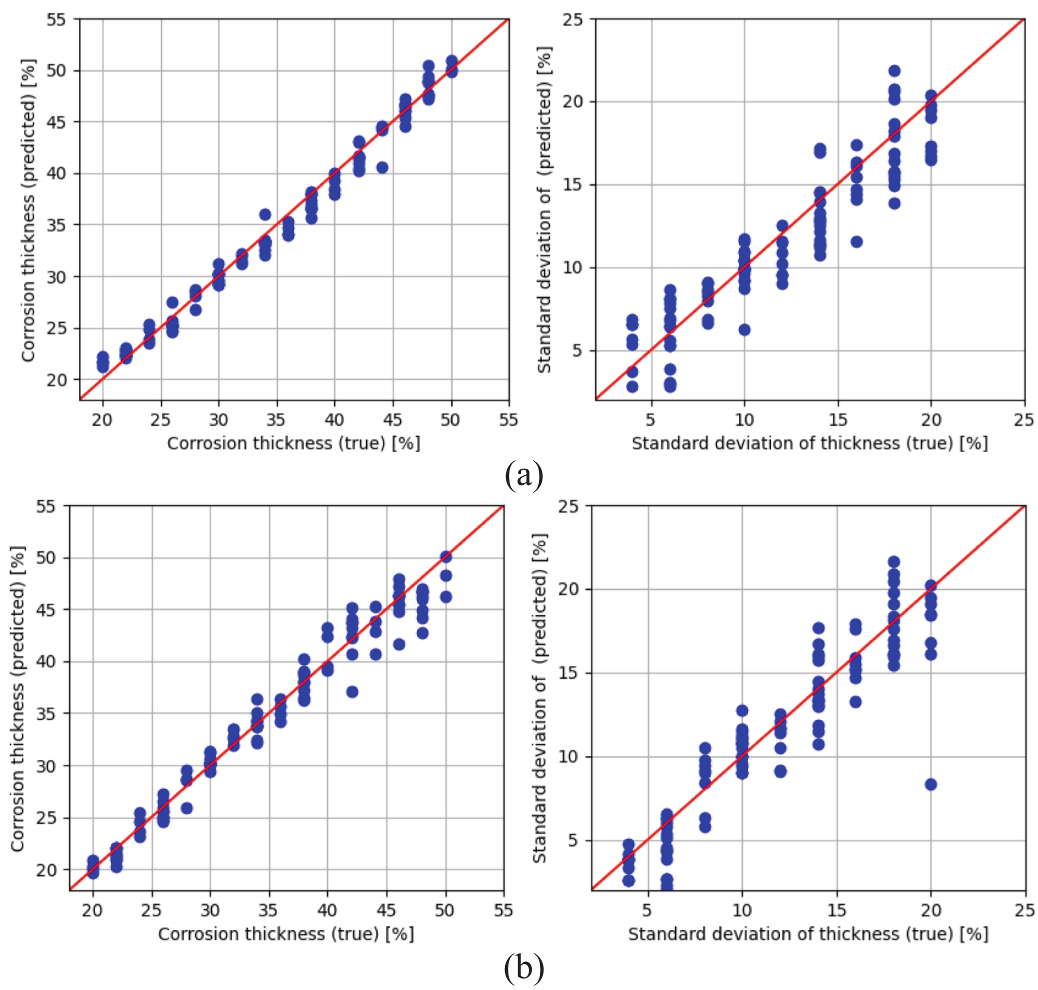

Fig. 12. Scatter plots for the corrosion parameter prediction techniques based on inverse model (multi-random-field approach with $N_f = 3$): (a) linear model, (b) quadratic model). The solid line indicates the identity function.

reduction and 7.0% for the standard deviation, while the MAE reaches only 0.5% and 0.9%, respectively. The correlation coefficients equal 0.997 for h and 0.975 for s, which indicates near-perfect prediction for thickness reduction and exceptionally strong predictive performance also for the roughness-related parameter.

From a physical standpoint, the observed improvement associated with increasing N_f can be interpreted in terms of sampling multiple effective propagation scenarios. Each realization of the stochastic corrosion field corresponds to a different spatial arrangement of local thickness variations. Consequently, the wave interacts with a different

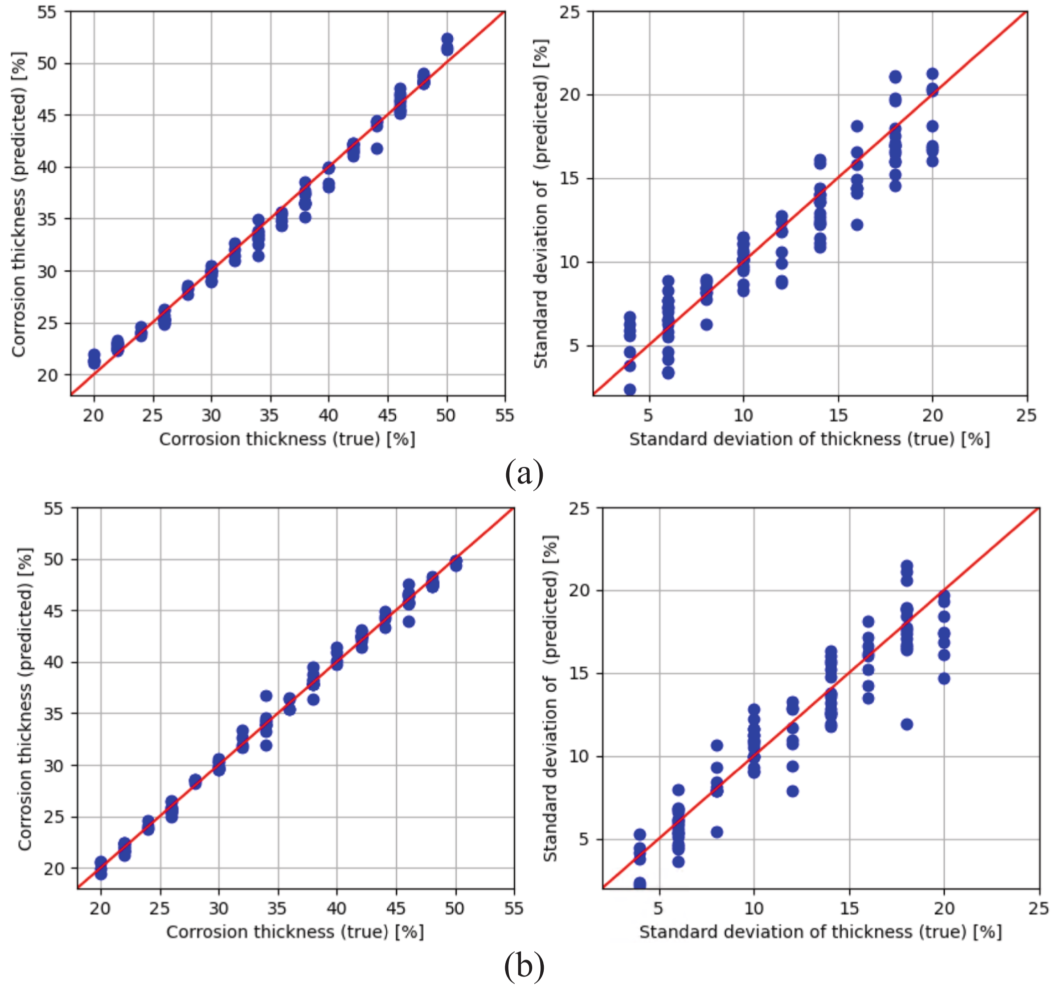

Fig. 13. Scatter plots for the corrosion parameter prediction techniques based on inverse model (multi-random-field approach with $N_f = 5$): (a) linear model, (b) quadratic model). The solid line indicates the identity function.

sequence of local geometrical features along the source–sensor trajectory, which affects the measured signal through changes in delay, attenuation, pulse broadening, and scattering. When only a single realization is used, the inverse model is forced to learn from data that contains a strong realization-dependent component. In contrast, averaging over several realizations suppresses this component and emphasizes those response characteristics that are consistently related to the global parameters h and s. This explains why the inverse mapping becomes more stable as the number of realizations increases.

The obtained results also provide further insight into the relative difficulty of estimating the two corrosion parameters. In all cases, the thickness reduction h is identified more accurately than the standard deviation s. This is consistent with the physical interpretation of the signal features. The mean corrosion level primarily affects the overall propagation delay and therefore has a strong and relatively direct influence on the extracted wave packet location. By contrast, the standard deviation is related to local roughness, which influences the signals in a more indirect and distributed manner, mainly through scattering, attenuation, and waveform distortion. As a consequence, s is inherently more difficult to identify and requires richer information content in the training data, as well as stronger averaging of stochastic variability.

The results also highlight the limitations of conventional ToF-based approaches. As discussed in Section 2.6, such methods effectively provide a path-averaged estimate of thickness and are therefore unable to represent the full spatial complexity of distributed corrosion. In structures with stochastic thickness variations, different propagation directions may lead to different effective velocities and thus different inferred thicknesses, even when the underlying global corrosion parameters remain the same. This directional inconsistency is reflected in the observed asymmetry of the recorded waveforms and explains why ToF-based methods are fundamentally limited in the present application.

From a practical perspective, the proposed methodology offers a realistic route toward experimental implementation. Although the present study uses multiple stochastic field realizations generated numerically, their physical counterpart may be interpreted as multiple measurements corresponding to slightly different source–sensor configurations. In practice, this can be achieved by repositioning sensors, shifting the excitation point, or performing measurements for several neighboring trajectories across the same inspected area. Even small modifications of the measurement configuration alter the effective thickness distribution encountered along the propagation path and thus provide additional information about the stochastic character of the corrosion field. In this sense, the proposed multi-random-field framework is not merely a numerical device, but a practically meaningful strategy for improving the reliability of corrosion assessment in real inspection scenarios.

4. Conclusion

This work presented a novel inverse modeling framework for the identification of global corrosion parameters in metallic plates, based on

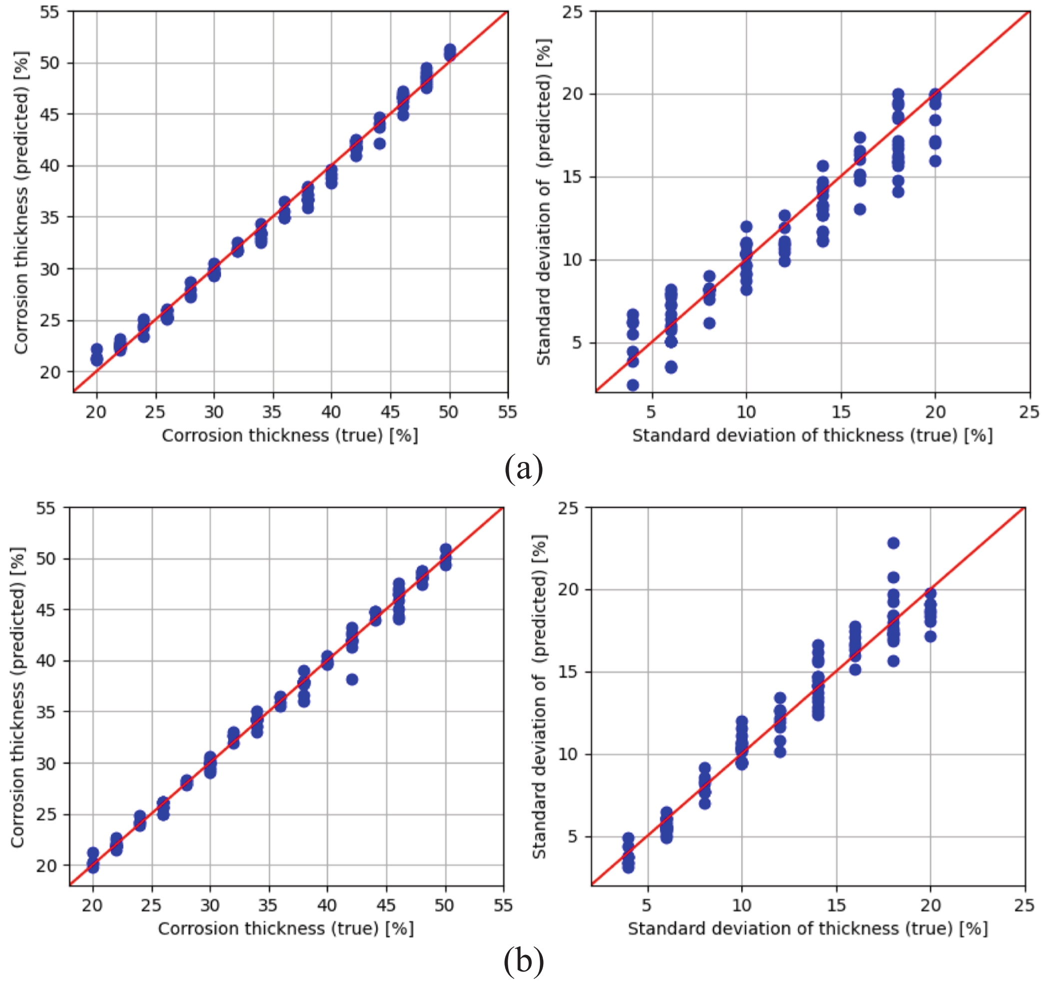

Fig. 14. Scatter plots for the corrosion parameter prediction techniques based on inverse model (multi-random-field approach with $N_f = 10$): (a) linear model, (b) quadratic model). The solid line indicates the identity function.

guided wave responses and multi-random-field modeling. By representing corrosion morphology as a stochastic field and combining this description with data-driven surrogate models, the proposed approach enables reliable estimation of both mean thickness reduction and its spatial variability. A key aspect of the study is the explicit treatment of the inherent non-uniqueness of the inverse problem. Instead of attempting to reconstruct a single realization of the corrosion field, the proposed methodology focuses on identifying its global statistical descriptors. The introduction of the multi-random-field strategy allows for effective mitigation of non-uniqueness by aggregating information from multiple realizations corresponding to the same parameter set. This leads to a more stable and well-conditioned inverse mapping between guided wave response features and corrosion parameters.

The obtained results demonstrate that the proposed approach consistently outperforms conventional time-of-flight-based identification methods. In particular, it enables significantly improved estimation accuracy while avoiding simplifying assumptions related to uniform thickness or path-averaged wave propagation. The study also shows that increasing the number of realizations used in the model construction leads to substantial improvements in predictive performance. From a methodological standpoint, the work confirms that relatively simple surrogate models, such as linear regression, can provide robust and accurate predictions when combined with appropriate data regularization. At the same time, more flexible models can further enhance performance, provided that sufficient information is available through multi-realization averaging.

An important advantage of the proposed framework is its clear physical interpretability and practical applicability. Although the methodology is formulated in terms of stochastic field realizations, its experimental counterpart can be naturally implemented by performing measurements for different source-sensor configurations. In this context, repositioning sensors or modifying excitation locations effectively corresponds to sampling different propagation paths and, consequently, different realizations of the thickness distribution encountered by the wave. This makes the proposed approach directly applicable in real-world inspection scenarios without requiring reconstruction of the full corrosion field. In practical applications, additional environmental and operational factors, such as temperature variations, sensor coupling conditions, contamination, and medium properties, may also influence guided wave propagation and should therefore be incorporated in future experimental investigations.

It is also worth noting that, in the present study, the guided wave excitation was limited to a single frequency. This can be considered a practical advantage, as it simplifies both the measurement setup and data interpretation. The selected excitation frequency was not arbitrary, but rather based on prior analyses indicating its suitability for capturing thickness-related effects in the considered configuration. At the same time, the choice of excitation parameters constitutes an additional degree of freedom that may further enhance the performance of the proposed framework. In particular, the future investigation of optimal excitation frequency or multi-frequency excitation strategies could provide improved sensitivity to different aspects of corrosion morphology, especially with respect to parameters related to spatial variability.

Ethical Statement

The authors state that the research was conducted according to ethical standards.

CRediT authorship contribution statement

Slawomir Koziel: Writing – review & editing, Writing – original draft, Visualization, Validation, Software, Methodology, Investigation, Funding acquisition, Formal analysis, Conceptualization. **Anna Pietrenko-Dabrowska:** Writing – review & editing, Writing – original draft, Software, Project administration, Methodology, Investigation, Formal analysis, Conceptualization. **Beata Zima:** Writing – review & editing, Writing – original draft, Visualization, Validation, Software, Methodology, Investigation, Conceptualization.

Declaration of competing interest

The authors declare that they have no known competing financial interests or personal relationships that could have appeared to influence the work reported in this paper.

Acknowledgements

This work was supported in part by the Icelandic Research Fund Grant 2410297 and by the National Science Centre of Poland Grant 2025/57/B/ST7/00738. Abaqus calculations were carried out at the Academic Computer Centre in Gdansk.

Data availability

Data will be made available on request.

References

[1] V. Giurgiutiu, Structural Health Monitoring of Aerospace Composites (2015), https://doi.org/10.1016/C2012-0-07213-4.
[2] P. Cawley, Guided waves in long range nondestructive testing and structural health monitoring: Principles, history of applications and prospects, NDT & E International 142 (2024) 103026, https://doi.org/10.1016/J.NDTEINT.2023.103026.
[3] J.L. Rose, P.B. Nagy, Ultrasonic Waves in Solid Media, J. Acoust. Soc. Am. 107 (2000), https://doi.org/10.1121/1.428552.
[4] J.D. Achenbach, S.A. Thau, Wave Propagation in Elastic Solids, J. Appl. Mech. 41 (1974), https://doi.org/10.1115/1.3423344.
[5] Z. Sun, Y. Zhu, X. Bai, Z. Qi, N. Hu, Precise identification of pipeline surface defects utilizing ultrasonic guided wave technology and data-driven algorithmic approaches, Journal of Pipeline Science and Engineering (2025) 100390, https://doi.org/10.1016/j.jpse.2025.100390.
[6] X. Yuan, W. Li, M. Deng, Quantitative assessment of corrosion-induced wall thinning in L-shaped bends using ultrasonic feature guided waves, Thin-Walled Struct. 196 (2024) 111493, https://doi.org/10.1016/J.TWS.2023.111493.
[7] A. Gajdacsi, F. Cegla, The effect of corrosion induced surface morphology changes on ultrasonically monitored corrosion rates, Smart Mater. Struct. 25 (2016), https://doi.org/10.1088/0964-1726/25/11/115010.
[8] R.C. Sriramadasu, S. Banerjee, Y. Lu, Detection and assessment of pitting corrosion in rebars using scattering of ultrasonic guided waves, NDT & E International 101 (2019) 53–61, https://doi.org/10.1016/J.NDTEINT.2018.10.005.
[9] A. Farhidzadeh, S. Salamone, Reference-free corrosion damage diagnosis in steel strands using guided ultrasonic waves, Ultrasonics 57 (2015) 198–208, https://doi.org/10.1016/J.ULTRAS.2014.11.011.
[10] W. Li, Y. Cho, Quantification and imaging of corrosion wall thinning using shear horizontal guided waves generated by magnetostrictive sensors, Sens. Actuators A Phys. 232 (2015) 251–258, https://doi.org/10.1016/J.SNA.2015.06.008.
[11] S.G. Haslinger, M.J.S. Lowe, P. Huthwaite, R.V. Craster, F. Shi, Elastic shear wave scattering by randomly rough surfaces, J. Mech. Phys. Solids 137 (2020), https://doi.org/10.1016/j.jmps.2019.103852.
[12] F. Shi, Variance of elastic wave scattering from randomly rough surfaces, J. Mech. Phys. Solids 155 (2021), https://doi.org/10.1016/j.jmps.2021.104550.
[13] L. Li, P. Fromme, Mode conversion of fundamental guided ultrasonic wave modes at part-thickness crack-like defects, Ultrasonics 142 (2024) 107399, https://doi.org/10.1016/J.ULTRAS.2024.107399.
[14] N. Nurmalia, H. Nakamura, M. Ogi, K. Hirao, Nakahata, Mode conversion behavior of SH guided wave in a tapered plate, NDT and E Int. 45 (2012), https://doi.org/10.1016/j.ndteint.2011.10.004.
[15] B. Zima, K. Woloszyk, Y. Garbatov, Experimental and numerical identification of corrosion degradation of ageing structural components, Ocean Eng. 258 (2022) 111739, https://doi.org/10.1016/J.OCEANENG.2022.111739.
[16] L. De Marchi, A. Marzani, N. Speciale, E. Viola, Prediction of pulse dispersion in tapered waveguides, NDT and E Int. 43 (2010), https://doi.org/10.1016/j.ndteint.2009.12.004.
[17] B. Zima, Determination of stepped plate thickness distribution using guided waves and compressed sensing approach, Measurement (lond). 196 (2022), https://doi.org/10.1016/j.measurement.2022.111221.
[18] L. Moreau, J.-G. Minonzio, M. Talmant, P. Laugier, Measuring the wavenumber of guided modes in waveguides with linearly varying thickness, J. Acoust. Soc. Am. 135 (2014), https://doi.org/10.1121/1.4869691.
[19] B. Zima, J. Moll, Theoretical and experimental analysis of guided wave propagation in plate-like structures with sinusoidal thickness variations, Arch. Civ. Mech. Eng. 23 (2023), https://doi.org/10.1007/s43452-022-00564-9.
[20] B. Zima, K. Woloszyk, Y. Garbatov, Corrosion degradation monitoring of ship stiffened plates using guided wave phase velocity and constrained convex optimization method, Ocean Eng. 253 (2022), https://doi.org/10.1016/j.oceaneng.2022.111318.
[21] B. Zima, J. Moll, Numerical and experimental investigation of guided ultrasonic wave propagation in non-uniform plates with structural phase variations, Ultrasonics 128 (2023) 106885, https://doi.org/10.1016/J.ULTRAS.2022.106885.
[22] J. Bao, W. Zhou, A random field model of external metal-loss corrosion on buried pipelines, Struct. Saf. 91 (2021) 102095, https://doi.org/10.1016/J.STRUSAFE.2021.102095.
[23] B. Nie, D. Huang, Y. Wang, H. Chen, S. Xu, Corrosion characteristics and random field model of corroded cold-formed thin-walled steel, Case Stud. Constr. Mater. 22 (2025) e04855, https://doi.org/10.1016/J.CSCM.2025.E04855.
[24] B. Zima, E. Roch, Nondestructive global corrosion measurement using guided wavefield data, Measurement (lond). 235 (2024), https://doi.org/10.1016/j.measurement.2024.114949.
[25] M. Schmitz, J.Y. Kim, L.J. Jacobs, Machine and deep learning for coating thickness prediction using Lamb waves, Wave Motion 120 (2023) 103137, https://doi.org/10.1016/J.WAVEMOTI.2023.103137.
[26] C. Sbarufatti, G. Manson, K. Worden, A numerically-enhanced machine learning approach to damage diagnosis using a Lamb wave sensing network, J. Sound Vib. 333 (2014) 4499–4525, https://doi.org/10.1016/J.JSV.2014.04.059.
[27] S.H.M. Rizvi, M. Abbas, Lamb wave damage severity estimation using ensemble-based machine learning method with separate model network, Smart Mater. Struct. 30 (2021), https://doi.org/10.1088/1361-665X/ac2e1a.
[28] Z. Yang, H. Yang, T. Tian, D. Deng, M. Hu, J. Ma, D. Gao, J. Zhang, S. Ma, L. Yang, H. Xu, Z. Wu, A review on guided-ultrasonic-wave-based structural health monitoring: from fundamental theory to machine learning techniques, Ultrasonics 133 (2023) 107014, https://doi.org/10.1016/J.ULTRAS.2023.107014.
[29] D. Benstock, F. Cegla, M. Stone, The influence of surface roughness on ultrasonic thickness measurements, J. Acoust. Soc. Am. 136 (2014) 3028–3039, https://doi.org/10.1121/1.4900565.
[30] C. Yang, Q. Shi, B. Lin, K. Hu, F. Zhu, Regularization method for load reconstruction with hybrid uncertainties based on interval theory and convex model theory, J. Sound Vib. 619 (2025) 119389, https://doi.org/10.1016/J.JSV.2025.119389.
[31] W.P. Zhang, X.L. Gu, Q.Q. Yu, J. Chen, Random field analysis of corrosion of steel in the artificial marine atmosphere, in: Life-Cycle of Structures and Infrastructure Systems - Proceedings of the 8th International Symposium on Life-Cycle Civil Engineering, IALCCE 2023, 2023. DOI: 10.1201/9781003323020-359.
[32] Â.P. Teixeira, C.G. Soares, Ultimate strength of plates with random fields of corrosion, Struct. Infrastruct. Eng. (2008), https://doi.org/10.1080/15732470701270066.
[33] K. Deliang, N. Biao, X. Shanhua, Random Field Model of Corroded Steel Plate Surface in Neutral Salt Spray Environment, KSCE J. Civ. Eng. 25 (2021), https://doi.org/10.1007/s12205-021-1249-5.
[34] Y. Liu, J. Li, S. Sun, B. Yu, Advances in Gaussian random field generation: a review, Comput. Geosci. 23 (2019), https://doi.org/10.1007/s10596-019-09867-y.
[35] C. Yang, Y. Xia, A multi-objective optimization strategy of load-dependent sensor number determination and placement for on-orbit modal identification, Measurement (lond). 200 (2022), https://doi.org/10.1016/j.measurement.2022.111682.
[36] C. Yang, Load-Dependent Structural State Reconstruction-Oriented and Reliability-based Sensor Placement Optimization Method, AIAA J. (2025), https://doi.org/10.2514/1.j065285.
[37] C. Yang, K. Liang, X. Zhang, X. Geng, Sensor placement algorithm for structural health monitoring with redundancy elimination model based on sub-clustering strategy, Mech. Syst. Signal Process. 124 (2019) 369–387, https://doi.org/10.1016/J.YMSSP.2019.01.057.
[38] H. Lamb, On the vibrations of an elastic sphere, Proceedings of the London Mathematical Society s1-13 (1881). DOI: 10.1112/plms/s1-13.1.189.